

THE X-SHOOTER GTO SAMPLE OF GRB AFTERGLOW AND HOST GALAXY SPECTRA

J. SELSING¹, D. MALESANI¹, P. GOLDONI¹⁴, T. KRÜHLER¹, J. P. U. FYNBO¹, A. DE UGARTE POSTIGO¹¹, J. JAPPEL²⁰, P. D'AVANZO, Z. CANO, S. COVINO¹⁰, V. D'ELIA^{7, 12}, H. FLORES, O. E. HARTOOG⁶, J. HJORTH¹, P. JAKOBSSON⁵, A. LEVAN, A. MELANDRI, S. PIRANOMONTE⁷, R. SÁNCHEZ-RAMÍREZ¹¹, S. SCHULZE^{17, 18}, N. R. TANVIR¹⁹, C. THÖNE, S. D. VERGANI^{7, 8}, P. M. VREESWIJK³, D. J. WATSON¹, K. WIERSEMA¹⁹, D. XU¹, L. CHRISTENSEN¹, A. DE CIA³, L. KAPER⁶, L. A. ANTONELLI, F. FIORE, A. GOMBOC, P. GROOT, F. HAMMER, C. LEDOUX², E. MAIORANO, B. MILVANG-JENSEN¹, E. PALAZZI, E. PIAN, J. SCHAYE, G. TAGLIAFERRI⁷, R. A. M. J. WIJERS⁶

Draft version October 26, 2016

ABSTRACT

The *Swift* satellite allows us to use gamma-ray bursts (GRBs) to peer into the hearts of star forming galaxies through cosmic time. Our open collaboration, representing most of the active ESO member researchers in this field, seeks to build a public legacy sample of GRB X-shooter spectroscopy while *Swift* continues to fly. We propose to continue our programme to target all suitably observable GRB afterglows (up to 15 bursts per semester), with the primary goal of producing a well-defined, homogeneous, statistically useful sample. To date, our spectroscopy covers a redshift range from 0.059 to about 8, with more than 20 robust metallicity measurements from absorption lines (over the redshift range 1.7–5.9) and 4 secure detections of H₂ or CH molecular absorption. Such information is extremely difficult to obtain by other means. In terms of studying the spread and redshift evolution in gas-phase properties, the sample is still limited by low-number statistics.

Keywords: Gamma-ray burst: individual: GRB 120815A — galaxies: high-redshift — ISM: molecules — dust, extinction

1. INTRODUCTION

Only after observing more than 12000 damped Lyman- α absorbers (DLAs) towards about 10⁵ QSOs have 5 systems with log($N_{\text{HI}}/\text{cm}^{-2}$) > 22 been identified (Noterdaeme et al.

2012, A&A, 547, L1). Long GRB afterglow spectra, by contrast, reveal such systems in the majority of cases (e.g., Jakobsson et al. 2006, A&A, 460, L13; Fynbo et al. 2009, ApJS, 185, 526). Whereas DLAs towards QSOs are mostly limited to $1.8 \lesssim z \lesssim 5$ due to the atmospheric UV-cutoff and increasing Lyman-blanketing at increasing redshifts (e.g., Rafelski et al. 2014, ApJL, 782, L29), GRBs allow us to see into the hearts of star-forming galaxies over the full history of cosmic star formation from $z \approx 0$ to $z > 8$ (e.g., Tanvir et al. 2009, Nature, 461, 1254; Salvaterra et al. 2009, Nature, 461, 1258; Jakobsson et al. 2012, ApJ, 752, 62). With afterglow spectroscopy (throughout the electromagnetic spectrum from X-rays to the sub-mm) we can hence characterize the properties of star-forming galaxies over cosmic history in terms of redshifts, metallicities, molecular contents, ISM temperatures, UV-flux densities, etc.. This is, however, only possible as long as there are satellites in orbit that rapidly and accurately locate GRBs. The currently operating *Swift* satellite, launched in 2004 and still fully-functioning, allows for very efficient follow-up observations of GRBs due to its unprecedented rate, speed and precision of localisations.

The case for a large sample of GRBs with X-shooter spectroscopy.

There are several unanswered but fundamental questions that must be addressed in order to exploit the full potential of GRBs as cosmological probes. More than 50% of the *Swift* bursts with measured redshift are at $z > 2$, and 5–10% are expected to be above $z = 5$ (Salvaterra et al. 2008, MNRAS, 380, L45; Salvaterra et al. 2012, ApJ, 749, 68; Jakobsson et al. 2012, ApJ, 752, 62; Perley et al. 2016, ApJ, 817, 7). A high redshift completeness is crucial for our understanding of the link between the number density of GRBs per unit redshift and the global star-formation history of the Universe, as measured by other means (UV, FIR, sub-mm, see Robertson & Ellis 2011, ApJ, 744, 95). The detection of GRBs at $z > 6$ shows that GRBs have become competitive as a tool to identifying galaxies at the highest redshifts and unsurpassed in providing detailed abundance information via absorption line spectroscopy (Tanvir et al. 2012, ApJ, 754, 46, McGuire

[†] Based on observations collected at the European Southern Observatory, Paranal, Chile, Program ID: 084.A-0260, 085.A-009, 086.A-0073, 087.A-0055.

¹ Dark Cosmology Centre, Niels Bohr Institute, University of Copenhagen, Juliane Maries Vej 30, 2100 København Ø, Denmark

² European Southern Observatory, Alonso de Córdova 3107, Vitacura, Casilla 19001, Santiago 19, Chile

³ Department of Particle Physics and Astrophysics, Faculty of Physics, Weizmann Institute of Science, Rehovot 76100, Israel

⁴ Thüringer Landessternwarte Tautenburg, Sternwarte 5, 07778 Tautenburg, Germany

⁵ Centre for Astrophysics and Cosmology, Science Institute, University of Iceland, Dunhagi 5, IS-107 Reykjavik, Iceland

⁶ Astronomical Institute Anton Pannekoek, University of Amsterdam, Science Park 904, NL-1098 XH Amsterdam, the Netherlands

⁷ INAF-Osservatorio Astronomico di Roma, Via Frascati 33, I-00040 Monteporzio Catone, Italy

⁸ GEPI-Observatoire de Paris, CNRS UMR 8111, Univ. Paris-Diderot, 5 Place Jules Janssen - 92190 Meudon, France

⁹ American River College, Physics and Astronomy Dpt., 4700 College Oak Drive, Sacramento, CA 95841, USA

¹⁰ INAF, Osservatorio Astronomico di Brera, Via E. Bianchi 46, I-23807 Merate, Italy

¹¹ Instituto de Astrofísica de Andalucía (IAA-CSIC), Glorieta de la Astronomía s/n, 18008, Granada, Spain

¹² ASI-Science Data Centre, Via Galileo Galilei, I-00044 Frascati, Italy

¹³ Institute of Experimental and Applied Physics, Czech Technical University in Prague, Horská 3a/22, 128 00 Prague 2, Czech Republic

¹⁴ APC, Astroparticules et Cosmologie, Université Paris Diderot, CNRS/IN2P3, CEA/Irfu, Observatoire de Paris, Sorbonne Paris Cité, 10, Rue Alice Domon et Léonie Duquet, 75205 Paris Cedex 13, France

¹⁵ Max-Planck-Institut für extraterrestrische Physik, Giessenbachstraße, 85748 Garching, Germany

¹⁶ Università degli studi di Milano-Bicocca, Piazza della Scienza 3, 20126, Milano, Italy

¹⁷ Pontificia Universidad Católica de Chile, Departamento de Astronomía y Astrofísica, Casilla 306, Santiago 22, Chile

¹⁸ Millennium Center for Supernova Science

¹⁹ Department of Physics and Astronomy, University of Leicester, University Road, Leicester, LE1 7RH, UK

²⁰ University of Ljubljana, Department of Physics, Faculty of Mathematics & Physics, SI

et al. 2016, ApJ submitted, arxiv:1512.07808).

From March 2005 to March 2016 there have been about 350 *Swift* bursts complying with our sample selection criteria (see “Immediate objective”), and about half of them have measured redshifts. Among the latter subset, the team proposing these observations has measured about two thirds of the redshifts, mainly with FORS1/2 and X-shooter (see Fynbo et al. 2009, ApJS, 185, 526; Jakobsson et al. 2012, ApJ, 752, 62; Krühler et al. 2012, ApJ, 758, 46). Our current aim is to build a sample superior to our previous low-resolution survey (Fynbo et al. 2009, ApJS, 185, 526), both in terms of quantity and quality of the spectra. Our program started as guaranteed time observations during periods 84-91, and we have continued in open time since then.

X-shooter is in many ways the ideal GRB follow-up instrument and indeed GRB follow-up was one of the primary science cases behind the instrument design and implementation. Our program secures general purpose GRB afterglow spectroscopic follow-up that adds strong legacy value to the *Swift* GRB sample. Due to the wide wavelength range of X-shooter with the same observation cover molecular H_2 absorption near the atmospheric cut-off and all the strong emission lines from the host in the NIR arm (e.g., Friis et al., 2015, MNRAS, 451, 167). In general, the wide wavelength coverage ensures that we always have features on which to base a redshift measurement as long as the afterglow is brighter than about 23 mag in either the R - or z -band. Frequently, emission lines are also detected from the underlying host, which also provide further information such as SFR and metallicity (the top right panel in Fig. 1 shows an example). Only for 7 out of more than 70 secured spectra could we not measure a redshift. With the X-shooter survey we provide **metallicity measurements** for about 30% (Voigt-profile fits) of the $z > 1.7$ events. So far we have measured metallicities for more than 20 GRB afterglows with X-shooter. With the wide wavelength coverage of X-shooter we can study important chemical species as Zn II, Cr II and α elements over a much wider redshift range than what is possible with other instruments. As an example, we have measured a metallicity of $0.1Z_{\odot}$ for GRB 100219A at $z = 4.669$ (Thöne et al. 2013, MNRAS, 428, 3590), $0.02Z_{\odot}$ for GRB 111008A at $z = 4.991$ (Sparre et al. 2014, ApJ, 785, 150) and $0.05Z_{\odot}$ for the $z = 5.9125$ GRB 130606A (Hartoog et al. 2015, A&A, 580, 139). Reconciling the abundance patterns of GRB absorbers, other types of absorbers, QSO DLAs in particular, and old stars in the Local Group is an important long-term goal (see also Sparre et al. 2014, ApJ, 785, 150). Metallicities are also measured from host emission lines (Krühler et al. 2015, A&A, 581, A125). GRB spectroscopy also allows us to determine the dust content of their environments, both through analysis of the depletion pattern and through measurement of the associated extinction (Japelj et al. 2015, A&A, 451, 2050). This allows us to quantify the dust-to-metals ratio and its evolution with redshift (e.g., De Cia et al. 2013, A&A, 560, 88; Zafar & Watson 2013, A&A, 560, 26).

We will also determine the frequency and properties of **molecular absorption** towards GRB absorbers. Molecular gas is a key element to catalyze the process of star formation, but prior to our program H_2 had been detected just in two cases (tentatively in Fynbo et al. 2006, A&A, 451, L47; securely in Prochaska et al. 2009, ApJ, 691, L27). With our X-shooter program we have found three more systems (Krühler et al. 2013, A&A, 557, 18; D’Elia et al. 2014, A&A, 564,

38; Friis et al. 2015, MNRAS, 451, 167). We are currently analysing more of our spectra for less obvious molecular absorption and we expect to find more (a dedicated sample paper is addressing this issue).

A natural question to ask is: **how long should this work continue?** Our view is that we need to keep observing the afterglows as long as we have *Swift* in operation. Also note that the program is still producing many papers and provides data for many theses (Box 9 and 10). *Swift* is currently funded until 2018, but is likely to get more extensions given its overwhelming success. As mentioned above GRBs allow us to probe star-forming galaxies that are almost impossible to study in other ways both in terms of redshifts, galaxy luminosity function, and regions within galaxies. After 7 periods we have secured seven spectra of $z > 4$ GRBs, of which three were of sufficient quality to allow abundance measurements (Thöne et al. 2013, Sparre et al. 2014, Hartoog et al. 2015). GRBs offer the only way to derive chemical abundances for the gas phase of central, actively star-forming regions of high- z galaxies. The program also maintains a very high discovery potential where we occasionally find something completely unexpected that provides interesting clues to puzzles in other fields, e.g. extinction of type Ia supernovae (Fynbo et al. 2014, A&A, 572, 12). Each of these spectra are like precious jewels – it is a type of observation that can never be repeated and a class of sightlines that can only be studied while we have operating GRB satellites.

It is also worth adding that we have build up a rather unique team spread over Europe from Granada to Reykjavik, which by now has reached a point where the distribution of night shifts, the scientific exploitation of the data is efficient and where we are open to all new members who wish to participate. As mentioned all data are public immediately.

For all of these reasons, we need to keep building up the sample of GRB afterglow spectra now as we may have to wait many years before a mission like *Swift* becomes available again.

A significant proportion of GRBs lack a bright optical afterglow (“**dark bursts**”, e.g., Jakobsson et al. 2004, ApJ, 617, L21; Melandri et al. 2012, MNRAS, 421, 1265). Some of these are at the highest redshifts ($z > 6$) and their observer-frame optical emission is absorbed by the IGM. The majority, however, suffer from large dust obscuration (e.g., Perley et al. 2009, AJ, 138, 1690; Greiner et al. 2011, A&A, 526, 30). Identifying such GRBs is important for constraining the fraction of obscured star formation. In both cases, NIR emission is expected. X-shooter can adequately study these objects, provided that a NIR counterpart is timely identified, for which we have the dedicated HAWKI run D.

The detection of **absorption line variability** can reveal the burst influence on the surrounding medium and in turn the absorber distance from the burst and its metallicity (Vreeswijk et al. 2007, A&A 468, 83; D’Elia et al. 2009, ApJ, 694, 332; Thöne et al. 2011, MNRAS, 414, 479; De Cia et al. 2012, A&A, 545, 64; Hartoog et al. 2013). **Short GRBs** originate in a substantially different environment compared to long GRBs. Short GRBs may be related to the merging of compact binaries and the coalescence time can be long enough to allow the progenitor system to move far away from the star formation site (Belczynski et al. 2002, ApJ, 571, 147). Up to now, however, no spectrum with a sufficient signal-to-noise ratio of a short GRB afterglow has been secured. A knowledge of the redshift distribution of short bursts is of key importance for

the next generation of gravitational wave experiments, as they are the likely EM counterparts to their primary targets.

2. SAMPLE SELECTION CRITERIA

Being of transient nature, it is difficult to impose strong sample selection criteria on GRBs, without hampering the follow-up effort. Many natural follow-up restrictions exist from already, being it weather conditions, pointing restrictions of the telescope or poorly localized bursts as reported by the *Swift*-telescope. To maximize the return of the follow-up campaign we have chosen a few selection criteria that attempts to provide an unbiased selection of bursts, while allowing for a high success-rate

²²

1. GRB triggered onboard by Swift.
2. Galactic $A_V \lesssim 0.5$ mag.
3. XRT started observing within 10 minutes since the GRB; an XRT position must be distributed within 12 hr.
4. The target must be visible for at least 60 min at least 30° above horizon, with the Sun below -12° .
5. No bright closeby stars.

A significant fraction of the bursts presented here

Insert exact number

have already had their hosts investigated in Krühler et al. (2015), for which extractions of the hosts exist. The focus of the data presented here are on the afterglows themselves and in the absence of a clear afterglow, the host. We will not, however, investigate the hosts.

²²Note that in the P84 proposal the criteria have been stated a bit differently, the visibility constraint being replaced by a declination + Sun angle constraint. The above criteria are however those defining the sample.

3. OBSERVATIONS

3.1. *RRM observations*

The rapid-response mode is

4. REDUCTION SCHEME

In cases where multiple traces are visible in the slit, additional components for the profile are used in the optimal extraction. The additional components share the PSF parameters and in cases where the additional component is an extended object, the fits have been inspected to ensure that the additional component does not skew the fit towards a broader

PSF. The additional components are not used for the weights.

Additionally, the wavelength solution for all bursts have been re-calibrated. Using a synthetic sky spectrum (Noll et al. 2012; Jones et al. 2013), a first refinement of the wavelength solution have been obtained by cross-correlating with the observed sky.

Both a multiplicative and an additive offset has been tested, but in terms of χ^2 , the model with only a multiplicative offset is preferred.

5. RESULTS

Table 1

The full sample of afterglows or hosts observed in the program. We here list the burst names and details of the spectroscopic observations. The exposure times and slit widths are given in the order UVB/VIS/NIR. The column Δt shows the time after trigger when the spectroscopic observation was started. Mag_{acq} gives the approximate magnitude (typically in the *R*-band) of the afterglow in the acquisition image.

GRB	Exptime (ks)	Slit width (arcsec)	Airmass	Seeing (arcsec)	Δt (hr)	Mag_{acq}	Redshift	Ref
GRB090313 ¹	6.9/6.9/6.9	1.0/0.9/0.9	1.2–1.4	1.0	45	21.6	3.3736	(1)
GRB090530 ¹	4.8/4.8/4.8	1.0/1.2/1.2	1.6–2.2	1.5	20	22	1.266	(2)
GRB090809 ¹	7.2/7.2/7.2	1.0/0.9/0.9	1.2–1.1	0.9	10.2	21	2.737	(2,3)
GRB090926 ¹	7.2/7.2/7.2	1.0/0.9/0.9	1.4–1.5	0.9	22	17.9	2.1062	(4)
GRB091018	2.4/2.4/2.4	1.0/0.9/0.9	2.1–1.8	0.8	3.5	19.1	0.9710	(5)
GRB091127	6.0/6.0/6.0	1.0/0.9/0.9	1.1–1.2	1.0	101	21.2	0.490	(6)
GRB100205A	10.8/10.8/10.8	1.0/0.9/0.9	1.9–1.8	1.0	71	–	–	(2)
GRB100219A	4.8/4.8/4.8	1.0/0.9/0.9	1.3–1.1	0.7	12.5	23	4.667	(7)
GRB100316B	2.4/2.4/2.4	1.0/0.9/0.9	2.0–2.4	0.7	0.7	18.2	1.18	(2)
GRB100316D-1 ²	3.6/3.6/1.8	1.0/0.9/0.9	1.2–1.3	1.0	10	21.5	0.059	(8)
GRB100316D-2	2.4/2.4/2.4	1.0/0.9/0.9	1.1–1.2	1.0	58	20.2	0.059	(8)
GRB100316D-3	2.6/2.6/3.2	1.0/0.9/0.9	1.1–1.2	1.1	79	19.9	0.059	(8)
GRB100316D-4	2.6/2.6/3.2	1.0/0.9/0.9	1.1–1.2	1.2	101	19.9	0.059	(8)
GRB100418A-1	4.8/4.8/4.8	1.0/0.9/0.9	1.6–1.3	0.7	8.4	18.1	0.624	(9)
GRB100418A-2	4.8/4.8/4.8	1.0/0.9/0.9	1.2–1.3	0.6	34	19.2	0.624	(9)
GRB100418A-3	4.8/4.8/4.8	1.0/0.9/0.9	1.2–1.4	0.7	58	–	0.624	(9)
GRB100424A ³	4.8/4.8/4.8	1.0/0.9/0.9	1.1–1.2	0.8	–	–	2.465	(2)
GRB100425A	2.4/2.4/2.4	1.0/0.9/0.9	1.5–1.3	0.7	4.0	20.6	1.755	(2,3)
GRB100615A ³	4.8/4.8/4.8	1.0/0.9/0.9	1.0–1.1	0.8	–	–	1.398	(2)
GRB100621A	2.4/2.4/2.4	1.0/0.9/0.9	1.3–1.4	1.0	7.1	–	0.542	(2)
GRB100625A ³	4.8/4.8/4.8	1.0/0.9/0.9	1.1–1.0	0.8	13	–	0.452	(2)
GRB100724A ⁴	4.2/4.2/4.2	1.0/0.9/0.9	1.5–2.3	0.7	0.2	–	1.288	(2)
GRB100728B ⁵	7.2/7.2/7.2	1.0/0.9/0.9	1.5–1.1	0.5	22	23	2.106	(2)
GRB100814A-1 ⁴	0.9/0.9/0.9	1.0/0.9/0.9	1.9–1.7	0.5	0.9	19	1.439	(2)
GRB100814A-2	4.8/4.8/2.4	1.0/0.9/0.9	1.5–1.2	0.6	2.1	19	1.439	(2)
GRB100814A-3	4.8/4.8/2.4	1.0/0.9/0.9	1.2–1.0	0.6	98	20	1.439	(2)
GRB100816A ⁶	4.8/4.8/2.4	1.0/0.9/0.9	1.8–1.6	0.8	28.4	–	0.805	(2)
GRB100901A	2.4/2.4/2.4	1.0/0.9/0.9	1.5–1.5	1.5	66	–	1.408	(10)
GRB101219A	7.2/7.2/7.2	1.0/0.9/0.9	1.1–1.7	2.0	3.7	–	0.718	(2)
GRB101219B-1	4.8/4.8/4.8	1.0/0.9/0.9	1.6–2.6	1.3	11.6	20	0.552	(11)
GRB101219B-2	7.2/7.2/7.2	1.0/0.9/0.9	1.2–2.0	0.8	394	22.7	0.552	(11)
GRB101219B-3	7.2/7.2/7.2	1.0/0.9/0.9	1.4–2.1	0.9	886	–	0.552	(11)
GRB110128A	7.2/7.2/7.2	1.0/0.9/0.9	2.0–1.6	0.9	5.5	22.5	2.339	(2)
GRB110407A	9.6/9.6/9.6	1.0/0.9/0.9	1.4–1.3	2.0	12.4	23	–	(2)
GRB110709B ^{1, 3}	7.2/7.2/7.2	1.0/0.9/0.9	1.6–1.1	1.0	–	–	–	(2)
GRB110715A	0.6/0.6/0.6	1.0/0.9/0.9	1.1–1.1	1.7	12.3	18.5	0.82	(2)
GRBGRB110808A	2.4/2.4/2.4	1.0/0.9/0.9	1.2–1.1	1.1	3.0	21.2	1.3488	(2)
GRB110818A	4.8/4.8/4.8	1.0/0.9/0.9	1.3–1.3	1.0	6.2	22.3	3.36	(2)
GRB111005A ³	1.2/1.2/1.2	1.0/0.9/0.9	1.3–1.3	0.7	–	–	0.013?	(2)
GRB111008A-1	8.8/8.8/8.4	1.0/0.9/0.9	1.1–1.0	1.2	8.5	21?	4.9898	(12)
GRB111008A-2	8.0/8.0/7.2	1.0/0.9/0.9	1.3–1.0	1.0	20.1	22?	4.9898	(12)
GRB111107A	4.8/4.8/4.8	1.0/0.9/0.9	1.8–1.5	0.7	5.3	21.5	2.893	(2)
GRB111117A ⁶	4.8/4.8/4.8	1.0/0.9/0.9	1.5–1.4	0.6	38	–	1.3?	(2)
GRB111123A-1	6.2/6.6/6.6	1.0/0.9/0.9	1.6–1.1	1.0	12.2	>24	3.1516	(2)
GRB111123A-2 ³	2.4/2.4/2.4	1.0/0.9/0.9	1.0–1.0	0.5	–	–	3.1516	(2)
GRB111129A	3.6/3.6/3.6	1.0/0.9/0.9	1.6–2.1	1.7	–	–	–	(2)
GRB111209A-1	4.8/4.8/4.8	1.0/0.9/0.9	1.1–1.2	0.8	17.7	20.1	0.677	(13)
GRB111209A-2	9.6/9.6/9.6	1.0/0.9/0.9	1.2–2.0	0.8	497	23	0.677	(13)
GRB111211A ¹	2.4/2.4/2.4	1.0/0.9/0.9	1.4–1.6	0.6	31	19.5	0.478	(2)
GRB111228A	2.4/2.4/2.4	1.0/0.9/0.9	1.4–1.4	0.9	15.9	20.1	0.716	(2)
GRB120118B ³	3.6/3.6/3.6	1.0/0.9/0.9	1.1–1.0	1.0	–	–	2.943	(2)
GRB120119A-1	2.4/2.4/2.4	1.0/0.9/0.9	1.1–1.1	0.6	1.4	17	1.728	(2)

Table 1 — *Continued*

GRB	Exptime (ks)	Slit width (arcsec)	Airmass	Seeing (arcsec)	Δt (hr)	Mag _{acq}	Redshift	Ref
GRB120119A-2	1.2/1.2/1.2	1.0/0.9/0.9	1.8–1.9	0.6	4.5	20	1.728	(2)
GRB120119A-3 ³	4.8/4.8/4.8	1.0/0.9/0.6JH	1.0–1.1	1.1	—	—	1.728	(2)
GRB120211A-1	4.8/4.8/4.8	1.0/0.9/0.9	1.1–1.4	1.0	—	—	2.346	(2)
GRB120211A-2	3.6/3.6/3.6	1.0/0.9/0.9	1.1–1.2	1.3	—	—	2.346	(2)
GRB120224A	2.4/2.4/2.4	1.0/0.9/0.9	1.7–2.1	1.4	19.8	22.3	1.10	(2)
GRB120311A ¹	2.4/2.4/2.4	1.0/0.9/0.9	1.6–1.4	0.6	3.7	21.6	0.350	(2)
GRB120327A-1	2.4/2.4/2.4	1.0/0.9/0.9	1.6–1.4	0.5	2.1	18.8	2.815	(14)
GRB120327A-2	4.2/4.2/4.2	1.0/0.9/0.9	1.0–1.1	1.0	29	22.5	2.815	(14)
GRB120404A	9.6/9.6/9.6	1.0/0.9/0.9JH	1.7–1.3	1.3	15.7	21.3	2.876	(2)
GRB120422A	4.8/4.8/4.8	1.0/0.9/0.9	1.3–1.3	0.6	16.5	22.0	0.283	(15)
GRB120712A	4.8/4.8/4.8	1.0/0.9/0.9	1.5–2.5	1.3	10.4	21.5	4.175	(2)
GRB120714B	4.8/4.8/4.8	1.0/0.9/0.9JH	1.5–1.2	1.2	7.8	22.1	0.398	(2)
GRB120716A ¹	3.6/3.6/3.6	1.0/0.9/0.9JH	1.8–2.6	1.0	62	20.9	2.486	(2)
GRB120722A ²	4.8/4.8/4.8	1.0/0.9/0.9	1.3–1.3	1.1	10.3	23.6	0.959	(2)
GRB120805A ²	3.6/3.6/3.6	1.0/0.9/0.9JH	1.3–1.7	0.9	218	—	2.8?	(2)
GRB120815A	2.4/2.4/2.4	1.0/0.9/0.9	1.3–1.4	0.6	1.69	18.9	2.358	(16)
GRB120909A	1.2/1.2/1.2	1.0/0.9/0.9	1.6–1.6	1.4	1.7	21	3.929	(2)
GRB120923A	9.6/9.6/9.6	1.0/0.9/0.9JH	1.2–1.4	1.0	18.5	—	≥ 8	(2)
GRB121024A	2.4/2.4/2.4	1.0/0.9/0.9	1.2–1.1	0.6	1.8	20	2.300	(17)
GRB121027A	8.4/8.4/8.4	1.0/0.9/0.9	1.3–1.3	0.9	69.4	21.15	1.773	(2)
GRB121201A	4.8/4.8/4.8	1.0/0.9/0.9JH	1.1–1.1	0.9	12.9	23	3.385	(2)
GRB121229A	4.8/4.8/4.8	1.0/0.9/0.9JH	1.4–1.2	1.4	2.0	21.5	2.707	(2)
GRB130131B ³	7.2/7.2/7.2	1.0/0.9/0.9JH	1.3–1.6	0.8	—	—	2.539	(2)
GRB130408A	1.2/1.2/1.2	1.0/0.9/0.9	1.0–1.0	1.0	1.9	20	3.758	(2)
GRB130418A	1.2/1.2/1.2	1.0/0.9/0.9	1.4–1.3	1.3	4.6	18.5	1.218	(2)
GRB130427A	1.2/1.2/1.2	1.0/0.9/0.9JH	1.8–1.8	0.8	16.5	19	0.340	(18)
GRB130427B	1.2/1.2/1.2	1.0/0.9/0.9JH	1.2–1.0	0.8	20.3	22.7	2.78	(2)
GRB130603B ⁶	2.4/2.4/2.4	1.0/0.9/0.9	1.4–1.4	1.1	8.2	21.5	0.356	(19)
GRB130606A	4.2/4.2/4.2	1.0/0.9/0.9JH	1.7–1.9	1.1	7.1	19	5.91	(20)
GRB130612A	1.2/1.2/1.2	1.0/0.9/0.9	1.3–1.3	1.4	1.1	21.5	2.006	(2)
GRB130615A	1.2/1.2/1.2	1.0/0.9/0.9	2.1–2.2	1.0	0.8	21	3?	(2)
GRB130701A	1.2/1.2/1.2	1.0/0.9/0.9JH	2.0–2.0	1.6	5.5	19.9	1.155	(2)
GRB160804A-1	2.4/2.4/2.4	1.0/0.9/0.9JH	1.3–1.4	—	22.4	Daniele?	0.736	(2)
GRB160804A-2 ³	3.6/3.6/3.6	1.0/0.9/0.9JH	1.8–1.9	—	—	—	0.736	(2)
GRB161007A ³	2.4/2.4/2.4	1.0/0.9/0.9JH	1.5–1.7	0.8	323	Daniele?	???	(2)
GRB161014A	4.8/4.8/4.8	1.0/0.9/0.9JH	1.1–1.2	0.6	11.6	Daniele?	2.823	(2)
Friis et al. (2015)								

References. — (1) de Ugarte Postigo et al. (2010); (2) This work ; (3) Skuladottir (2010); (4) D’Elia et al. (2010); (5) Wiersema et al. (2012); (6) Vergani et al. (2011); Cobb et al. (2010); (7) Thone et al. (2013); (8) Bufano et al. (2012) ; (9) De Ugarte Postigo et al. (2011) ; (10) Hartoog et al. (2013); (11) Sparre et al. (2011); (12) Sparre et al. (2014); (13) Levan et al. (2014); (14) D’Elia et al. (2014); (15) Schulze et al. (2014); (16) Krühler et al. (2013); (17)

¹ Not part of the statistical sample

² Spectrum dominated by light from the host galaxy

³ Spectrum of the host galaxy taken long after the burst

⁴ RRM observation

⁵ ADC malfunction during observation

⁶ Short burst

5.1. Spectral resolution

The afterglow spectra described in this paper are obtained in Target-of-Opportunity (override) mode. In most cases there is therefore little possibility to tweak slit widths to the seeing at the time of observations (i.e. to optimise spectral resolution and signal to noise), and almost all our data is therefore taken with a fixed set of slit widths and binning, described above. In a fair number of cases, the seeing full width at half maximum (FWHM) is considerably smaller than the slit width, and the delivered spectral resolution will then be determined by the seeing rather than slit width, as afterglows are point sources (this is evidently not the case for extended sources, e.g for host galaxies). The delivered resolution for slit width dominated spectra post-reduction and extraction can easily be determined from the bright sky emission lines. For

afterglow spectra with very high signal to noise, the delivered spectral resolution can at times be determined from the science data themselves. However, in the presence of multiple velocity components in absorption, other forms of line broadening, and a lack of lines at some redshifts, this is difficult to do at poorer signal to noise ratios (the majority of spectra in our sample). A broad starting value for the expected resolution will help fitting of these spectra, and can be important in upper limit determination, and for this reason we construct a aim to construct a crude relation between the seeing and the delivered resolution at our slit width, binning, and reduction pipeline settings. To this end we use observations of telluric standard stars that are taken with identical instrument settings as our afterglow spectra, usually just after the science data, as part of the ESO X-shooter calibration plan. These spectra have been reduced together with the afterglow spectra, using identical pipeline settings with the same version of the pipeline. First we fit a Gaussian function in the spatial direction of the trace of the standard star at 792 nm (i.e. in the VIS arm). After this, we fit a series of 20 telluric absorption lines in the telluric standard star spectra with Gaussians, taking care to select transitions that are not almost-resolved multiples, should be intrinsically unresolved, and are in areas with well defined continuum flux. We pick 34 telluric standard stars spanning a range of DIMM seeing values, with the majority between 0.5–1.5 arcsec. The resulting distribution of spectral FWHM (km/s) as a function of spatial FWHM at 792 nm is fairly well described by a linear relation $a + b * x$, with

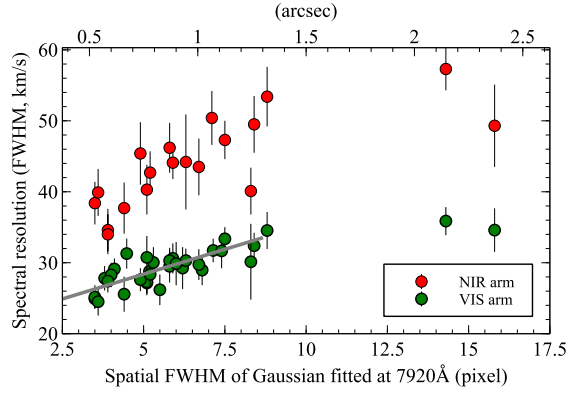


Figure 1. Green datapoints show the FWHM (km/s) of Gaussian fits to unresolved telluric absorption lines in the VIS spectra, as a function of the FWHM of a Gaussian fit onto the trace in spatial direction at 792 nm. The lower horizontal axis is in units pixels, the top axis in arc seconds. The red datapoints show a subsample of NIR spectra. The grey line shows a linear fit to the VIS datapoints.

x the spatial FWHM in pixels (with 0.15 arc sec per pixel), $a = 21.4 \pm 1.3$ km/s, $b = 1.4 \pm 0.2$. We use this linear relation as a way to estimate the spectral resolution for medium to poor signal to noise afterglow spectra in the VIS arm. To extend this to the UVB and NIR arm, we measured a series of lines in NIR arm spectra of a subset of 19 sources used for the VIS arm above, and find that the resulting distribution is consistent with a simple scaling of the VIS arm relation by the ratio of resolutions of the NIR and VIS arm for unresolved, slit filling, sources as given on the ESO instrument website. The UVB arm contains no suitable absorption lines to use, and we therefore use a scaled value as in the NIR arm. While this simple method is not terribly accurate (for one, the spatial profile of the trace is not a perfect Gaussian), but it gives a sufficiently accurate estimate for the analysis of these poor signal to noise science spectra.

5.2. Correction for offsets in the wavelength calibration

X-shooter, being installed at the VLT Cassegrain focus is prone to flexures during operations. The flexures modify the projection of the slit on the detector with respect to the one obtained in daytime calibration. This requires a modification of the wavelength solution in order to process correctly the night-time data. Part of this correction is performed by the pipeline using the frames taken during X-shooter Active Flexure Compensation procedure²³ We corrected the remaining part using as a reference the sky emission lines present in the observed data.

For every afterglow observation we reduced one frame individually in STARE mode without sky subtraction obtaining ~ 100 sky spectra. The sky line list compiled at ESO for the E-ELT study²⁴ from the work of (Hanuschik, 2003, A&A, 407, 1157) and (Rousselot et al. (2000, A&A, 354, 1134), was used as a reference. From this list, we selected a subset of bright and isolated lines. In the case of the OH doublets, unresolved at X-shooter resolution, we took as line position the average between the blue and red components. To find the offsets of the spectra, we fitted gaussians near the expected positions under IDL using the MPFIT software (Markwardt,

2009, Astronomical Society of the Pacific Conference Series, Vol. 411, ADASS XVII, ed. D.A. Bohlender, D. Durand, & P. Dowler, 251) and we compared the result to the tabulated values. The resulting offsets, which were smaller than 0.1 Å in the UVB and VIS data and smaller than 0.5 Å in the NIR spectra, were applied to the corresponding spectra.

5.3. Redshifts

6. DISCUSSION

JPUF, BMJ and DX acknowledge support from the ERC-StG grant EGG-278202. The Dark Cosmology Centre is funded by the Danish National Research Foundation. TK acknowledges support by the European Commission under the Marie Curie Intra-European Fellowship Programme in FP7. AdUP acknowledges support by the European Commission under the Marie Curie Career Integration Grant programme (FP7-PEOPLE-2012-CIG 322307). This work made use of data supplied by the UK *Swift* Science Data Centre at the University of Leicester. Finally, we acknowledge expert support from the ESO staff at the Paranal and La Silla observatories in obtaining these target of opportunity data.

REFERENCES

- Bufano, F., Pian, E., Sollerman, J., et al. 2012, *Astrophys. J.*, 753, 67
Cobb, B. E., Bloom, J. S., Perley, D. A., et al. 2010, *Astrophys. J.*, 718, L150
De Ugarte Postigo, A., Thöne, C. C., Goldoni, P., & Fynbo, J. P. U. 2011, *Astron. Nachrichten*, 332, 297
de Ugarte Postigo, A., Goldoni, P., Thöne, C. C., et al. 2010, *Astron. Astrophys.*, 513, A42
D’Elia, V., & Stratta, G. 2011, *Astron. Astrophys.*, 532, A48
D’Elia, V., Fynbo, J. P. U., Covino, S., et al. 2010, *Astron. Astrophys.*, 523, A36
D’Elia, V., Fynbo, J. P. U., Goldoni, P., et al. 2014, *Astron. Astrophys.*, 564, A38
Fong, W., Berger, E., Chornock, R., et al. 2013, *Astrophys. J.*, 769, 56
Friis, M., De Cia, A., Krühler, T., et al. 2015, *Mon. Not. R. Astron. Soc.*, 451, 167
Fynbo, J. P. U., Krühler, T., Leighly, K., et al. 2014, *Astron. Astrophys.*, 12, 1
Hartoog, O. E., Wiersema, K., Vreeswijk, P. M., et al. 2013, *Mon. Not. R. Astron. Soc.*, 430, 2739
Hartoog, O. E., Malesani, D., Fynbo, J. P. U., et al. 2015, *Astron. Astrophys.*, 580, A139
Jones, A., Noll, S., Kausch, W., Szyszka, C., & Kimeswenger, S. 2013, *Astron. Astrophys.*, 560, A91
Krühler, T., Ledoux, C., Fynbo, J. P. U., et al. 2013, *Astron. Astrophys.*, 557, A18
Krühler, T., Malesani, D., Fynbo, J. P. U., et al. 2015, *Astron. Astrophys.*, 581, A125
Levan, A. J., Tanvir, N. R., Starling, R. L. C., et al. 2014, *Astrophys. J.*, 781, 13
Noll, S., Kausch, W., Barden, M., et al. 2012, *Astron. Astrophys.*, 543, A92
Schulze, S., Malesani, D., Cucchiara, A., et al. 2014, *Astron. Astrophys.*, 102, 1
Sparre, M., Sollerman, J., Fynbo, J. P. U., et al. 2011, *Astrophys. J.*, 735, L24
Sparre, M., Hartoog, O. E., Krühler, T., et al. 2014, *Astrophys. J.*, 785, 150
Starling, R. L. C., Wiersema, K., Levan, A. J., et al. 2011, *Mon. Not. R. Astron. Soc.*, 411, 2792
Thone, C. C., Fynbo, J. P. U., Goldoni, P., et al. 2013, *Mon. Not. R. Astron. Soc.*, 428, 3590
Vergani, S. D., Flores, H., Covino, S., et al. 2011, *Astron. Astrophys.*, 535, A127
Wiersema, K., Curran, P. A., Krühler, T., et al. 2012, *Mon. Not. R. Astron. Soc.*, 426, 2

²³X-shooter User Manual available at <https://www.eso.org/sci/facilities/paranal/instruments/xshooter/doc.html>

²⁴http://www.eso.org/sci/facilities/eelt/science/drm/tech_data/data/optical_ir_sky_lines.pdf

APPENDIX

A. NOTES ON INDIVIDUAL OBJECTS

A.1. *GRB090313*A.2. *GRB100205A*

Observed 3 days after the *Swift* trigger. No afterglow or host detected in 10.8 ks. GRB likely located at high redshift²⁵. The spectrum has not otherwise been published previously.

A.3. *GRB100219A* ($z = 4.667$)

The data presented here also formed the basis of GCN # 10441²⁶ and is published in Thone et al. (2013). Observations started 12.5 hours after the *Swift* trigger and has a total exposure time of 4.8 ks. Absorption features, including those of Ly α , from a multitude of ions are detected against the afterglow continuum at $z = 4.667$. Additionally, absorption from an intervening system is found at $z = 2.181$.

A.4. *GRB100316B* ($z = 1.180$)

The data presented here also formed the basis of GCN # 10495²⁷. The spectrum has not otherwise been published previously. Observations started 44 minutes after the *Swift* trigger and has a total exposure time of 2.4 ks. Absorption features from Fe II, Al II, Al III, Mg II and Mg I are well detected against the afterglow continuum at $z = 1.180$. Additionally, strong absorption lines from Fe II and Mg II from an intervening system are found at $z = 1.063$.

A.5. *GRB100316D* ($z = 0.059$)

The data presented here also formed the basis of GCN # 10512²⁸, GCN # 10513²⁹, GCN # 10543³⁰ and is published in Bufano et al. (2012) and Starling et al. (2011). This GRB is very close by and has an associated SN, SN2010bh, and has therefore undergone intense follow-up. The data presented here consists of a subset of the entire VLT/X-shooter campaign, covering the four first observing days while the afterglow still contributes significantly to the total emission. The first observations started 10 hours after the burst, before the SN was discovered, and targeted the star-forming 'A'-region(Starling et al. 2011), not the GRB. A very rich spectrum containing a multitude of emission lines puts the host at $z = 0.059$. For three consecutive nights, 58, 79 and 101 hours after the *Swift* trigger, the afterglow was observed as it transitioned into the spectrum of a high-velocity Ic-BL SN. The observations taken 79 and 101 hours after the burst are taken under programme 084.D-0265(A) (PI: Benetti), but with an identical setup to the first two observations.

A.6. *GRB100418A* ($z=0.624$)

The data presented here also formed the basis of GCN # 10620³¹ and GCN # 10631³² and is published in De Ugarte Postigo et al. (2011). The burst have been followed up in three epochs of observations, 0.4, 1.4, and 2.4 days after the burst, each lasting 4.8 ks. The unambiguous redshift of the host, $z = 0.624$, is found from the simultaneous detection of emission features belonging to nebular lines, including H I, [O II], [O III], [Ne III], [N II], [S II], [S III], and [He I] as well as absorption features due to the presence of Zn II, Cr II, Fe II, Mn II, Mg II, Mg I, Ti II, and Ca II, all at a consistent redshift. Temporal evolution of the fine-structure lines belonging to Fe II* is found between the epochs.

A.7. *GRB100424A* ($z=2.465$)

The data presented here also formed the basis of GCN # 14291³³. The spectrum has not otherwise been published previously. Observations carried out, long after the burst has faded. Emission lines from the host are detected at $z = 2.465$.

A.8. *GRB100425A* ($z=1.1755$)

The data presented here also formed the basis of GCN # 10684³⁴ and is used in ?, but not published elsewhere. Observations started 4 hours after the *Swift* trigger, totaling 2.4 ks. Absorption features from Mg II and Fe II in the afterglow continuum are detected at $z = 1.1755$.

A.9. *GRB100615A* ($z=1.398$)

The data presented here also formed the basis of GCN # 14264³⁵, but not published elsewhere. Host observation of a dark burst(D'Elia & Stratta 2011) taken long after the afterglow has faded. Emission lines from the host belonging to [O II], [Ne III], [O III] and H α are detected at a common redshift of $z = 1.398$.

²⁵<http://gcn.gsfc.nasa.gov/gcn3/10399.gcn3>

²⁶<http://gcn.gsfc.nasa.gov/gcn3/10441.gcn3>

²⁷<http://gcn.gsfc.nasa.gov/gcn3/10495.gcn3>

²⁸<http://gcn.gsfc.nasa.gov/gcn3/10512.gcn3>

²⁹<http://gcn.gsfc.nasa.gov/gcn3/10513.gcn3>

³⁰<http://gcn.gsfc.nasa.gov/gcn3/10543.gcn3>

³¹<http://gcn.gsfc.nasa.gov/gcn3/10620.gcn3>

³²<http://gcn.gsfc.nasa.gov/gcn3/10631.gcn3>

³³<http://gcn.gsfc.nasa.gov/gcn3/14291.gcn3>

³⁴<http://gcn.gsfc.nasa.gov/gcn3/10684.gcn3>

³⁵<http://gcn.gsfc.nasa.gov/gcn3/14264.gcn3>

A.10. *GRB100621A* ($z=0.542$)

The data presented here also formed the basis of GCN # 10876³⁶, but not published elsewhere. Beginning 7.1 hours after the GRB, 2.4 ks observations reveal emission lines from [O II], H β and [O III] at a common redshift of $z = 0.542$ and a very weak afterglow continuum.

A.11. *GRB100625A* ($z=0.452$)

The data presented here is of the candidate host galaxy, taken long after the burst has faded and have not previously been published. 4.8 ks of exposure reveals a weak continuum present in all arms, but an absence of emission lines. This could indicate that the host primarily contains a older stellar population. The redshift, $z = 0.452$, is taken from Fong et al. (2013).

A.12. *GRB100724A** ($z = 1.288$)

The data presented here also formed the basis of GCN # 10971³⁷. The spectrum has not otherwise been published previously. The observations were carried out in RRM starting 11 min after the GRB trigger. See section 3.1, for a description of the RRM scheme. Absorption lines from several ionic species are detected in the afterglow continuum at a common redshift of $z = 1.288$. This is not a part of the statistical sample.

A.13. *GRB100728B* ($z=2.106$)

The data presented here also formed the basis of GCN # 11317³⁸. The spectrum has not otherwise been published previously. Starting 22 hours after the burst trigger, 7.2 ks of observations reveals a faint afterglow continuum with Ly α - and Mg II-absorption at $z = 2.106$. Due to a malfunctioning ADC, the sensitivity of X-shooter is depressed with respect to normal operations, resulting in a poorer throughput. Additionally, the position of the trace on the slit moves due to atmospheric differential refraction.

A.14. *GRB100814A* ($z=1.439$)

The spectra presented here has not been published previously. The observations consists of three visits, the first beginning only 0.9 hours after the *Swift* trigger, the other two visits were 2.13 and 98.40 hours after the trigger, respectively. A bright afterglow continuum is present in all visits, allowing identification of absorption features belonging to a wide range of ions at $z = 1.439$. A complex velocity structure in the absorption features belonging to Mg II, shows several components, separated by as much as 500km/s, pointing to a likely merger scenario in the host.

A.15. *GRB100816A* ($z=0.805$)

The data presented here also formed the basis of GCN # 11123³⁹. The spectrum has not otherwise been published previously. This short GRB was observed 28.4 hours after the GRB trigger. 4 x 1200 s of exposure reveals two distinct sets of emission lines, spatially offset $\lesssim 1''$, very close in redshift space, $z = 0.8034$ and $z = 0.8049$, indicating either an interacting host or some complex velocity structure of the host. Faint underlying continua are present under both sets of lines.

A.16. *GRB100901A* ($z=1.408$)

The data presented here has been published in Hartoog et al. (2013). Because of the unusual lingering brightness of this GRB, 2.4s of observations taken 65.98 hours after the GRB trigger still reveals an afterglow continuum visible across the entire spectral coverage of X-shooter. Absorption lines from a wide range ion put the redshift at $z = 1.408$, with intervening absorption systems at $z = 1.3147$ and $z = 1.3179$.

A.17. *GRB101219A* ($z=0.718$)

This data has not been published before. Starting 3.7 hours after the GRB trigger, 7.2 ks of exposure time reveals a very faint continuum in the visual and near-infrared, only visible when heavily binning the images. No redshift estimate is available from these observations. Late-time Gemini-North observations reveal emission lines from the host at $z = 0.718$ ⁴⁰.

A.18. *GRB101219B* ($z=0.552$)

The data presented here also formed the basis of GCN # 11579⁴¹ and is published in Sparre et al. (2011). The first observation, taken 11.6 hours after the burst trigger and lasting 4.8ks, reveals absorption from Mg II and Mg I in the host located at $z = 0.552$ on a featureless continuum visible across the entire coverage of X-shooter. Subsequent observations taken 16 and 37 days after the trigger shows the fading spectral signature of a SN, SN2010ma.

A.19. *GRB120118B* ($z = 2.943$)

The data presented here also formed the basis of GCN # 14225⁴², but is not published otherwise. This late-time observation of the host of GRB120118B consists of 3.6 ks exposures and contains emission lines belonging to [O II] and [O III] at $z = 2.943$, suggested to be redshift of the host.

³⁶<http://gcn.gsfc.nasa.gov/gcn3/10876.gcn3>

³⁷<http://gcn.gsfc.nasa.gov/gcn3/10971.gcn3>

³⁸<http://gcn.gsfc.nasa.gov/gcn3/11317.gcn3>

³⁹<http://gcn.gsfc.nasa.gov/gcn3/11123.gcn3>

⁴⁰<http://gcn.gsfc.nasa.gov/gcn3/11518.gcn3>

⁴¹<http://gcn.gsfc.nasa.gov/gcn3/11579.gcn3>

⁴²<http://gcn.gsfc.nasa.gov/gcn3/14225.gcn3>

A.20. *GRB120119A* ($z = 1.728$)

The data presented here has not been published before. Three epochs of observations have been obtained, the first two immediately after the burst, and the last one long after the afterglow had faded. Starting 1.4 hours after the *Swift* trigger, the first epoch contains bright afterglow continuum. Rich in absorption features belonging to a multitude of ions, $z = 1.728$ is estimated for the host with intervening systems at $z = 1.476$, $z = 1.214$, $z = 0.662$ and $z = 0.632$. The second epoch, obtained 4.5 hours after the burst contains the fading afterglow. A third epoch is obtained > 1 year after the GRB in which emission lines from $H\beta$ and $H\alpha$ are found at the redshift of the host, confirming the association of the absorption line system and the host.

A.21. *GRB120211A* ($z = 2.346$)

The data presented here has been published in Krühler et al. (2015). Two observations of the host of GRB120211A has been obtained, starting 2013.02.17, > 1 year after the burst has faded. A redshift for this object has been reported by Krühler et al. (2015) and the features seen by those authors are reproduced in these reductions, confirming $z = 2.346$.

A.22. *GRB120224A* ($z = 1.10$ NEW!!!)

The data presented here has formed the basis of GCN # 12991⁴³, and has also been published in Krühler et al. (2015). Starting 19.8 hours after the GRB trigger, a total exposure time of 2.4 ks reveals a faint continuum, starting at ~ 7000 Å and extending all the way through 25000 Å. We detect a $\sim 2\sigma$ emission line which, if interpreted as $H\alpha$, gives $z = 1.10$, supporting the redshift reported by Krühler et al. (2015).

A.23. *GRB120311* ($z = 0.350$ NEW!!!)

The data presented here has formed the basis of GCN # 12991⁴⁴, but is not published otherwise. Starting just before twilight, 3.65 hours after the burst, a faint afterglow continuum is detected at all wavelengths. Due to the faintness of the afterglow, no absorption features are discernible superposed on the continuum. Displaced from the afterglow continuum by $1''.4$, emission lines belonging to $H\beta$, [O III] and $H\alpha$ are detected at $z = 0.350$. The line belonging to $H\alpha$ shows some extended emission toward the afterglow continuum. The angular distance between the two sources correspond to a projected distance in the host plane of 6 kpc, posing a potential problem for the host redshift, unless the GRB occurred in a merging system. The extended emission in $H\alpha$, supports this interpretation. This burst is not apart of the statistical sample.

A.24. *GRB120327A* ($z = 2.813$)

The data presented here also formed the basis of GCN # 13134⁴⁵ and is published in D'Elia et al. (2014). The observation consists of two visits, 2.13 hrs and 29.98 hrs after the burst, with an afterglow continuum visible in all arms for both visits. We detect absorption features from Ly-limit, $Ly\alpha$, C II/C II*, Si II/Si II*, Al I, Fe II and Mg II are detected at a consistent redshift, $z = 2.813$.

A.25. *GRB120404A* ($z = 2.876$)

The data presented here has formed the basis of GCN # 13227⁴⁶, but is not published otherwise. 9.6 ks integration, starting 15.7 hours after the *Swift*-trigger reveals a low-intensity afterglow continuum on which absorption from $Ly\alpha$ is detected in two distinct regions at redshifts $z = 2.876$ and $z = .255$. These absorption systems are confirmed by ionic absorption features at both of these redshifts.

A.26. *GRB120422A* ($z = 0.283$)

The data presented here also formed the basis of GCN # 13257⁴⁷ and is published in Schulze et al. (2014). A GRB-SN, this burst has been followed up multiple times. The data presented here only contain the first epoch in which the afterglow is still visible and before the rise of SN2012bz. Starting 16.5 hours after the burst, 4.8 ks integration time captures both the host and the burst in emission. A blue afterglow continuum is detected at all wavelengths covered by X-shooter, on which Mg II absorption at $z = 0.283$ is found. Offset by $1''.75$, the host is clearly detected at a consistent redshift with a rich emission line spectrum, the lines extending towards to burst.

A.27. *GRB120712A* ($z = 4.175$)

The data presented here also formed the basis of GCN # 13460⁴⁸ and is not published elsewhere. 4.8 ks integration time, starting 10.5 hours after the BAT trigger, shows a bright afterglow continuum starting at ~ 4720 Å, signifying the onset of the Lyman alpha forest, for a GRB located at $z = 4.175$. Absorption features from $Ly\alpha$, Fe II, Mg II and Si II are readily detected at a consistent redshift.

A.28. *GRB120714B* ($z = 0.398$)

The data presented here also formed the basis of GCN # 13477⁴⁹, but is not published elsewhere. Observations of this burst started 7.8 hours after the GRB trigger, lasting 4.8 ks. A continuum is visible across the entire spectral coverage of X-shooter, with both emission lines from [O II], $H\beta$, [O III] and $H\alpha$, as well as absorption from Mg II detected at $z = 0.398$, securely setting it as the redshift of the GRB.

⁴³<http://gcn.gsfc.nasa.gov/gcn3/12991.gcn3>

⁴⁴<http://gcn.gsfc.nasa.gov/gcn3/12991.gcn3>

⁴⁵<http://gcn.gsfc.nasa.gov/gcn3/13134.gcn3>

⁴⁶<http://gcn.gsfc.nasa.gov/gcn3/13227.gcn3>

⁴⁷<http://gcn.gsfc.nasa.gov/gcn3/13257.gcn3>

⁴⁸<http://gcn.gsfc.nasa.gov/gcn3/13460.gcn3>

⁴⁹<http://gcn.gsfc.nasa.gov/gcn3/13477.gcn3>

A.29. *GRB120716A* ($z = 2.486$)

The data presented here also formed the basis of GCN # 13494⁵⁰, but is not published elsewhere. Despite observations starting 62 hours after the *Swift* trigger and lasting 3.6 ks, a bright afterglow is clearly seen, along with a plethora of absorption features. Absorption of Ly α -photons in the host leaves a broad trough, from which the Lyman alpha forest is visible bluewards, all the way down to the Lyman limit. Metal absorption lines from C II, Si II, [O I], Fe II, C IV, Si IV, including fine structure transitions identified as C II*, Si II*, Fe II* and metastable [Ni II] lines are all detected at $z = 2.486$

A.30. *GRB120805A* ($z \sim 3.9$ NEW!!!)

A separate reduction of this burst has been published in Krühler et al. (2015), but not otherwise. Starting 9 days after the burst trigger, this is host observation and does not contain any afterglow continuum. In 3.6 ks integration time, we detect a faint continuum visible from 4500 Å and all the way through 21000 Å, in contrast to what is found previously. The continuum from 4500 - 6000 Å is detected at very low significance. If the drop at 4500 Å is the Lyman limit, this fits with Lyman alpha at ~ 6000 Å, giving $z \sim 3.9$. The absence of nebular lines if due to [O II] falling in a telluric absorption band and the rest being shifted out of the wavelength coverage.

A.31. *GRB120815A** ($z = 2.358$)

Not a part of the statistical sample, this burst also formed the basis of GCN # 13649⁵¹ and is published in Krühler et al. (2013). Observations started 1.69 hours after the BAT trigger and consist of 2.4 ks integration. A bright afterglow continuum is detected across the entire spectral coverage of X-shooter, with a multitude of absorption lines superposed. Absorption features from the host at $z = 2.358$ include a DLA as well as metal absorption lines from [N V], [S II], Si II, [O I], C IV, Si IV, Fe II, Al II, Al III, Mn II, Mg II, and Mg I. Additionally fine-structure lines from [Ni II] and Fe II are excited local to the GRB. Intervening systems are found at $z = 1.539$, $z = 1.693$, and $z = 2.00$.

A.32. *GRB120722A* ($z = 0.959$)

The data presented here also formed the basis of GCN # 13507⁵², but is not published elsewhere. On 4.8 ks integration time, starting 10 hours after the burst trigger, the simultaneous detection of absorption features belonging to Mg II and Fe II superposed on a blue continuum, and emission lines from [O II], H γ , H β , [O III] and H α , all at $z = 0.959$, confidently sets it as the redshift of the GRB.

A.33. *GRB120909A* ($z = 3.929$)

The data presented here has formed the basis of GCN # 13730⁵³, but is not published otherwise. A very rapid follow-up, starting only 1.7 hours after the BAT trigger, this 1.2 ks observation captures a very bright afterglow continuum, starting at 4500 Å, signifying the onset of the Lyman limit for a system at $z = 3.929$. Absorption from high-column density hydrogen leaves very prominent absorption features in the form of Ly α , Ly β , and Ly γ , visible in the Lyman alpha forest. Metal absorption lines arising from Fe II, [Ni II], Si II, [S II], Al II, Al III, C II, [O I], C IV, and Zn II are all detected along with the corresponding fine-structure lines from (Fe II*, Si II*, [O I]*, [O I]**, C II*), securely anchoring the redshift of the host.

A.34. *GRB121024A* ($z = 2.300$)

The data presented here also formed the basis of GCN # 13890⁵⁴ and is published in Friis et al. (2015). Also rapid, starting 1.8 hours after the *Swift* trigger, a bright afterglow continuum is visible across all arms. A broad absorption feature from Lyman alpha, along with narrow lines from C IV, Si II, Si IV, Fe II, [S II], and Al II, as well as fine-structure lines associated with Si II* are all detected at $z = 2.300$, securely setting it as the redshift of the GRB.

A.35. *GRB121027A* ($z = 1.773$)

The data presented here has formed the basis of GCN # 13930⁵⁵, but is not published otherwise. Starting 69.6 hours after the GRB trigger, that we detect the afterglow continuum a so high significance in all arms with 8.4 ks integration, testifies to the brightness of this burst. The concurrent identification of emission lines from [O III] and absorption from C IV, Al II, Al III, Mg I, Mg II, and Fe II, tightly constrains the redshift of the burst to be ($z = 1.773$)

A.36. *GRB130408A* ($z = 3.758$)

The data presented here also formed the basis of GCN # 14365⁵⁶. The spectrum has not otherwise been published previously. The observations consists of two 600sec spectra taken 1.9hrs after the burst. We detect absorption features from a wide range of ions. We also detect intervening absorption at $z = 1.255$ and $z = 3.248$.

A.37. *GRB130606A* ($z = 5.913$)

The data presented here also formed the basis of GCN # 14816⁵⁷ and is published in Hartoog et al. (2015). The observations consists of three 2x600sec visits starting 7.1 hrs after the burst at fairly high airmass. We detect absorption features from a wide range of ions at $z = 5.913$ as well as intervening absorption at $z = 2.3103, 2.5207, 3.4515, 4.4660, 4.5309, 4.5427, 4.6497$ and 4.7244 .

⁵⁰<http://gcn.gsfc.nasa.gov/gcn3/13494.gcn3>

⁵¹<http://gcn.gsfc.nasa.gov/gcn3/13649.gcn3>

⁵²<http://gcn.gsfc.nasa.gov/gcn3/13507.gcn3>

⁵³<http://gcn.gsfc.nasa.gov/gcn3/13730.gcn3>

⁵⁴<http://gcn.gsfc.nasa.gov/gcn3/13890.gcn3>

⁵⁵<http://gcn.gsfc.nasa.gov/gcn3/13930.gcn3>

⁵⁶<http://gcn.gsfc.nasa.gov/gcn3/14365.gcn3>

⁵⁷<http://gcn.gsfc.nasa.gov/gcn3/14816.gcn3>

A.38. *GRB151021A* ($z = 2.330$)

The data presented here also formed the basis of GCN # 18426⁵⁸ and is not published elsewhere. The observation was carried out in RRM starting 44 minutes after the GRB trigger. We detect absorption features from a wide range of ions at $z = 2.330$ as well as intervening absorption at $z = 1.49$.

A.39. *GRB160203A* ($z = 3.517$)

The data presented here also formed the basis of GCN # 18982⁵⁹ and is not published elsewhere. The observation was carried out in RRM starting 18 minutes after the GRB trigger. We detect absorption features from a wide range of ions at $z = 3.517$ as well as intervening absorption at $z = 2.203$.

A.40. *GRB160804A* ($z = 0.736$)

The data presented here also formed the basis of GCN # 19773⁶⁰, but is not published elsewhere. Observations started 22.37 hours after the BAT trigger and lasted for 2.4ks. The afterglow continuum is detected across the entire spectral coverage of X-shooter and absorption lines from Mg I, Mg II, Fe II and Al II are found at $z = 0.736$. At the same redshift, emission lines from [O II], [O III], H α , H β , H γ , [N II], [S II], [S III] are found. A second epoch, lasting 3.6ks, is obtained after the afterglow has faded, confirming the emission line detections.

A.41. *GRB161007A* ($z = 4.6$??? NEW!!!)

This data has not been published elsewhere. Observations for GRB161007A started 323 hours after the burst trigger and contains the potential host. 4 x 600 seconds of observations reveals a faint continuum rising abruptly above the noise at ~ 6850 Å and continuing through 21000 Å. A very low significance continuum is detected at shorter wavelengths, down to ~ 6000 Å. If the host is located at $z \sim 4.6$, the drop in continuum flux is the Lyman alpha break and the absence of nebular emission lines is due to [O II] being shifted out of the wavelength coverage. Alternatively, an early-type host at $z = 0.71$ could exhibit the 4000 Å break at 6000 Å, but due to the preference of long-duration GRBs for star-forming galaxies, this is the least likely explanation, why we believe the high- z solution.

A.42. *GRB161014A* ($z = 2.823$)

The data presented here also formed the basis of GCN # 20061⁶¹, but is not published elsewhere. Starting 11.6 hours after the GRB trigger, 4.8 ks of integration time captures the afterglow continuum across all three spectroscopic arms. A broad absorption trough due to Lyman alpha is visible, along with metal absorption features from Mg II, Si II, C II, C IV, Al II, Al III, and Fe II, all at $z = 2.823$. Similar to GRB140506 (Fynbo et al. 2014), a break in the continuum shape is detected bluewards of 6000 Å, possibly signifying some anomalous form of extinction.

⁵⁸<http://gcn.gsfc.nasa.gov/gcn3/18982.gcn3>

⁵⁹<http://gcn.gsfc.nasa.gov/gcn3/18982.gcn3>

⁶⁰<http://gcn.gsfc.nasa.gov/gcn3/19773.gcn3>

⁶¹<http://gcn.gsfc.nasa.gov/gcn3/20061.gcn3>